Original article

Microstructural characterisation of organic matter pores in coal-measure shale

Kunjie Li[1,6]*, Shaoqi Kong[2,3,4], Peng Xia[5], Xiaoling Wang[4,6]

[1]*Shanxi Provincial Guoxin Energy Development Group Company Limited, Taiyuan 030024, P. R. China*

[2]*Department of Energy and Power Engineering, Tsinghua University, Beijing 100084, P. R. China*

[3]*Shanxi Research Institute for Clear Energy Tsinghua University, Taiyuan 030032, P. R. China*

[4]*College of Mining Engineering, Taiyuan University of Technology, Taiyuan 030024, P. R. China*

[5]*College of Resource and enviornmental Engineering, Guizhou University, Guiyang 550025, P. R. China*

[6]*Shanxi Key Laboratory of Coal and Coal-measure Gas Geology, Taiyuan 030024, P. R. China*

Abstract:
To gain the insight into the nature of organic matter (OM) micro-nanometer pores and fractal features of coal-measure shale from the OM macromolecular evolution perspective, 28 Taiyuan formation shale samples are collected from Qinshui Basin and characterized with Rock-eval, Field emission scanning electron microscope (FE-SEM), low-pressure N_2 gas adsorption (Lp-N_2GA) and Fourier transform infrared spectroscopy (FTIR). The results show that OM is in the high-over mature stage. Pore size ranges from 5.7 to 26.7 nm and pores less than 4 nm are dominant. Two pore fractal dimensions D_1 and D_2 are obtained from Lp-N_2GA with the Frenkel-Halsey-Hill method, which are in the range of 2.272-2.617 and 2.561-2.799, respectively. A series of FTIR structure parameters are obtained by peak fitting the FTIR spectra to describe the microstructure of OM molecules, such as length of aliphatic chain, degree of aromatic carbon condensation and hydrocarbon generation potential. Micro-nanometer OM-related pores in FE-SEM images can be classified as OM hydrocarbon-generating pores, OM structure pores, OM intergranular pores and micro-cracks, with the first being most developed. Both hydrocarbon-generation and condensation of aromatic nucleus have positive effects on D_1. Hydrocarbon-generation is more effective for the development of micropores, while the condensation of aromatic nucleus is more conducive for the development of mesopores (<10 nm). The higher the total organic carbon content, and the more the micropores and mesopores (<10 nm) develop, the higher the value of D_1.

1. Introduction

As an important component of unconventional gas resource, the coal-measure shale gas has great potential for resource exploration and broad prospects for development in China. According to the assessment of the Ministry of Land of China in 2012, the exploitable resources for marine-continental transitional coal-measure shale gas are estimated to be 8.97×10^{12} m^3 (Wang, 2013; Dong et al., 2015; Zou et al., 2016, 2019). On the one hand, coal-measure shale deposits vertically with coal, sandstone and limestone, and the thickness for a single continuous deposition layer is generally less than 20 m, which is unfavorable for the exploration and development of coal-measure shale gas resources. But on the other hand, coal-measure shale is commonly mixed with thin coal-seams or coal-lines, which could greatly improve the hydrogen generation capacity of coal-measure shale system and is sufficient to make up for the shortcoming of small single layer thickness. Nowadays, the most feasible way to develop coal-measure shale gas is to co-exploit with coal-bed methane or tight sand gas, which is helpful to reduce the cost of deep coal-bed methane resource (buried depth >1000 m) development.

The pores' microscopic characteristics are the primary factors controlling the gas storage and flow mechanism for shale.

The space of macro pores and fractures define the amount of free gas, the nanometer pores and surface area influence the gas sorption capacity, and the shapes and connectivity of pores strongly affect permeability and gas flow ability (Jarvie et al., 2007; Roger and O'Brien, 2011; Curtis et al., 2012; Ko et al., 2017; Kong et al., 2019; Gao et al., 2020). The study of pore characteristics is beneficial to understand the generation, migration and storage mechanism of coal-measures shale gas. Approaches used to study the porosity of shale can be mainly classified into two categories: qualitative and quantitative identification. The micro-nanometer scale pore morphology and connectivity of shale can be intuitively observed with high resolution equipment, such as Field emission-scanning electron microscopy (FE-SEM), Transmission electron microscopy (TEM), X-ray computed tomography (X-CT) and atomic force microscopy (AFM) etc. The distribution characteristics of pores can also be analyzed with high resolution images (Jarvie et al., 2007; Gu et al., 2015; Abouelresh, 2017; Gou et al., 2019; Liu et al., 2019). The quantitative techniques mainly include intrusive methods and nonintrusive methods. The former is to inject non-wetting fluids into the shale sample and obtain the pore-related parameters by calculating the fluid injection amount under different pressures, such as pore surface area, pore volume and pore size distribution. The mercury injection capillary pressure (MICP), low-pressure N_2 and CO_2 gas adsorption are of this type (Gu et al., 2015; Sun et al., 2016; Zhang et al., 2016; Shao et al., 2017). The nonintrusive methods mainly refers to the nuclear magnetic resonance technology (NMR) (Fleury and Romero, 2016; Zhou et al., 2016), which is essential in obtaining pore structure parameters by analyzing the T_2 relaxation time with mathematical models. In many researches, the fractal dimensions have been used to quantitatively describe the fractal feature of micro-nanometer pores and fractures in shale, which can be obtained by the box-counting method based on high resolution images of FE-SEM and X-CT or with Frenkele-Halseye-Hill (FHH) model based on N_2 adsorption data (Loucks et al., 2009; Yang et al., 2016; Li et al., 2018). Both methods have proved to be effective in characterizing the heterogeneity and irregularity of pore systems in shale.

OM is a critical contribution to the development and evolution of pores, especially for secondary pores. The TOC, kerogen type and maturity all have influence on numbers and size distribution of nanometer pores in shale. Many studies have shown that nano-pores developed in local OM enriched area resulted from cracking of OM and hydrocarbon trapping, which accounted for up to 50% OM bulk (Loucks et al., 2009; Yang et al., 2016; Shao et al., 2017). Many researches have focused on the role of OM in pore structure by analyzing the correlation between OM parameters (such as TOC, OM maturity, etc.) and pore structure parameters (pore volume, surface area and pore fractal dimensions) (Bhargava et al., 2005; Sun et al., 2016; Yang et al., 2016; Ko et al., 2017; Shao et al., 2017; Li et al., 2018a, 2018b). However, the size of OM pores within shale is from micron to nanometer, and is dominated by nanometer, which falls into the range of OM macromolecular size and controlled by OM microstructure to a large extent. OM macromolecular evolution plays an essential role for OM pores. As a non-destructive testing technology, Fourier transform infrared spectroscopy (FTIR) has been widely used to reveal the structure and evolution of macromolecules in coal, oil shale and sandstone. The FTIR structure parameters of OM macromolecular, such as the size of aromatization, the length of aliphatic chain and hydrocarbon generation potential can be obtained with FTIR data. This can be used to describe the OM microstructure and evaluate OM thermal maturity (Pfeiferper and Avnir, 1983; Ibarra et al., 1996; Lis et al., 2005; Wang et al., 2011; Li et al., 2015; Craddock et al., 2017).

In this study, we collected Taiyuan Fomation (TYF) core samples from central-southern Qinshui Basin and applied the FTIR, Rock-eval, FE-SEM and low-pressure N_2 gas adsorption (Lp-N_2GA) to describe the OM macromolecular structure and pore structure of shale samples with different TOC. The effect of OM evolution on pores structure and fractal characteristics are discussed on the macromolecular scale.

2. Samples and methods

Qinshui Basin is one of the six major coalfields in Shanxi province and is the most successful area of the coal-bed methane commercial development in China. As the main coal-measure strata, the Carboniferous TYF is formed in a marine-continental transitional sedimentary environment and widely developed in Qinshui Basin with an average thickness of 100 m. The TYF shale is interceded with coal, sandstone and limestone with a thickness from several meters to 20 meters.

Twenty-eight TYF shale samples were collected from the drilled wells (Well TL-01, Well WX-01, and Well ZQ-01) in central-southern Qinshui Basin (Fig. 1) with a buried depth between 1100 and 1600 m. These samples are dark grey, gray-black and black (Fig. 2). The dark grey samples are mostly from the middle part of thick shale layer, whereas the gray-black and black shale are obtained from roof or floor of coal seam. Core samples were assessed with experiments of total organic carbon content (TOC) determination, Rock-eval, FTIR, FE-SEM observation and Lp-N_2GA.

TOC was measured with Chinese National Standard GB/T 19145-2003 on an Eltra CS-800 carbon-sulfur analyzer. The shale samples were crushed into powder with a particle size less than 150 μm. Inorganic carbon was removed with hydrochloric acid 5% concentration (Bhargava et al., 2005; Loucks et al., 2009; Yang et al., 2016).

A pyrolysis experiment was conducted on all samples with an YQ-VIIA pyrolyzer following China National standard GB/T 18602-2012. Samples were crushed to the grain size of 70-150 μm. The powder samples were heated to 300 °C and held for 3 mins, then heated to 600 °C at 25 °C/min. The parameters S_1, S_2, S_4 and T_{max} were obtained (Landais et al., 1997; Zhang et al., 2015).

The pore morphology of samples was observed using a Jeol 7610F and a Tescan MIRA 3 FE-SEM with an Energy-dispersive Spectrometers (EDS). The thin chips samples, with a size of 6-7 mm square and a thickness of 0.2-0.3 mm, were selected for FE-SEM observation. In this study, the samples were finely ground and polished, and then coated with gold
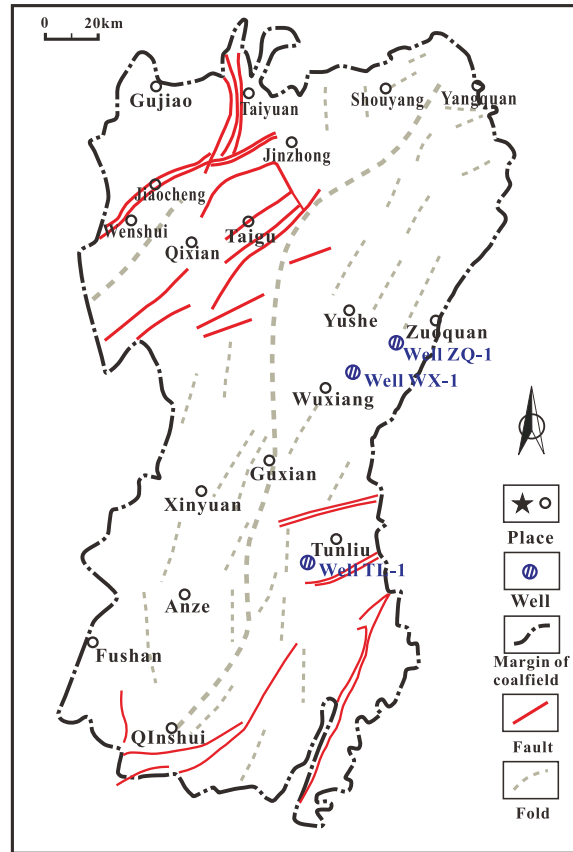
Fig. 1. Geological map of Qinshui basin and locations of drilled wells.
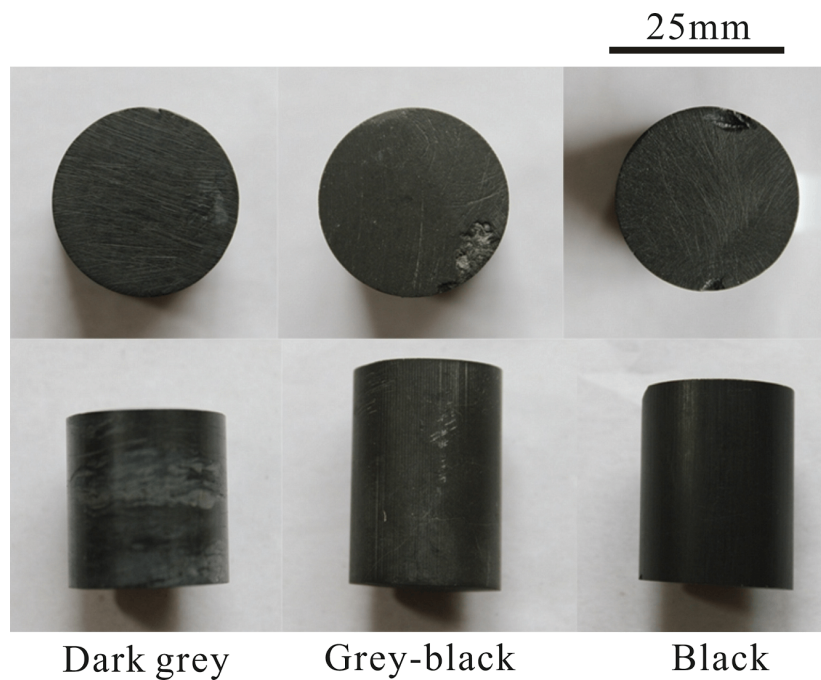
Fig. 2. Shale samples with different TOC.
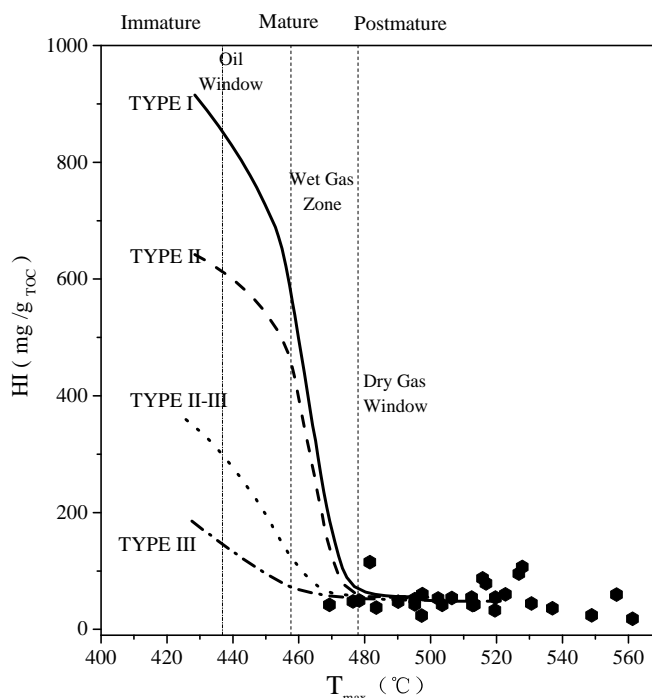
Fig. 3. Plot of T_{max} vs. HI.

to ensure the good conductivity.

The Lp-N_2GA test was conducted on a V-Sorb 2800TP surface area and pore size analyzer according to ASTM standard. Shale samples were crushed into powder with a size less than 150 μm and dehydrated for 12 h at 393 K in a fine vacuum to remove free and adsorbed water. At liquid nitrogen temperature (77 K), the N_2 adsorption-desorption isotherms were collected under relative pressures (P/P_o) from 0.01 to 0.99. Based on the N_2 adsorption data, the meso-macropore (>2 nm) surface area was evaluated by the multi-point method of Brunauer-Emmett-Teller (BET) in the P/P_o range of 0.05-0.30. The meso-macropore volume was obtained with the Barrette Joynere Halenda (BJH) method, and the micropores volume (0.64-2 nm) was determined applying the SF (Saito-Foley) model. Pore size distributions were determined using the BJH method with N_2 adsorption data (Jarvie et al., 2007; Sun et al., 2016; Zhou et al., 2016; Ko et al., 2017; Shao et al., 2017; Li et al., 2018a; Zou et al., 2019) .

The FTIR analysis was performed on a Bio-Rad FTS165. The spectra were collected in the region from 400 to 4000 cm^{-1} at 4 cm^{-1} resolution. All samples were firstly ground into powder and were degassed at 120 °C for 6-8 hours. Mixed with KBr according to the mass ratio of 100: 1, the shale powder samples were pressed into small chips under 10 Mpa for a minute.

The pore fractal dimensions based on N_2 adsorption data were calculated with FHH model, the equation is as follows (Pfeiferper and Avnir, 1983; Jaroniec and Avnir, 1989; Yang et al., 2014; Ji et al., 2016; Yang et al., 2016; Li et al., 2018b):

$$\ln V = K \ln \left(\ln \frac{P_o}{P} \right) + Constant \tag{1}$$

where V is the volume of N_2 adsorption under different equilibrium pressures P; K is the slope of the function obtained by linear fitting of the values of $\ln V$ and $\ln(\ln(P_o/P))$; P_o represents the saturated vapor pressure at 77 K. The fractal dimensions were calculated with the following equation:

$$D = K + 3 \tag{2}$$

The fractal dimensions are between 2 and 3, which represents totally smooth pore surfaces and completely irregular pore surface, respectively.

3. Results

3.1 Geochemical characterization

3.1.1 TOC and maturity

The results of the TOC and Rock-eval analysis are listed in Table 1. TOC values vary from 0.7% to 11.7% with an average value of 3.1%. 19 samples' TOC exceeds 2%, accounting for 68% of total samples.

As shown in Table 1, the $S_1 + S_2$ is between 0.17 and 1.52 mg/g with an average value of 0.59 mg/g. T_{max} varies from 469.3 to 561.3 °C with a mean value of 506.9 °C, indicating OM is in the high-over thermal mature stage (Landais et al., 1997; Zhang et at., 2015; Abouelresh 2017; Wood et al., 2018). The hydrogen index HI ranges from 17.9 to 114.9, implying OM is type III (humic) gas prone kerogen (Fig. 3).

3.1.2 FTIR spectra

The FTIR results of coal and coal-measure shale samples are shown in Fig. 4. The position, shape and trend of FTIR

Table 1. Geochemical data of shale samples.

Samples	Depth (m)	TOC (%)	S_1 (mg/g)	S_2 (mg/g)	T_{max}	HI (mg/g$_{TOC}$)	I_1	I_2	I_3	DOC_1	DOC_2	A
TL-01	1095.3	1.0	0.0048	0.22	469.3	42.1	–	–	–	–	–	–
TL-02	1102.5	2.0	0.0100	0.45	496.6	44.3	1.75	0.13	5.06	0.15	5.88	0.54
TL-03	1112.7	2.4	0.0166	0.44	483.5	37.1	2.16	0.27	8.72	0.56	18.35	0.68
TL-04	1118.4	0.6	0.0087	0.22	476.4	48.0	–	–	–	–	–	–
TL-05	1122.5	1.7	0.0101	0.24	497.3	23.7	1.47	0.25	13.19	0.19	10.22	0.44
TL-06	1131.6	6.2	0.0363	0.72	502.3	52.8	1.28	0.18	6.11	0.78	27.10	0.82
TL-07	1138.1	3.8	0.0190	0.88	516.8	78.6	1.51	0.16	6.06	0.35	12.88	0.68
TL-08	1143.5	1.7	0.0183	0.55	527.8	107.0	1.31	0.07	9.18	0.17	22.75	0.71
TL-09	1158.7	0.9	0.0151	0.26	519.5	32.6	–	–	–	–	–	–
TL-10	1169.2	5.1	0.0481	0.85	495.2	51.9	1.72	0.39	13.33	0.91	39.12	0.70
TL-11	1172.9	2.5	0.0166	0.50	503.5	42.0	1.47	0.21	3.81	0.29	5.35	0.58
TL-12	1178.3	3.4	0.0256	0.56	490.2	47.6	1.46	0.20	6.57	0.28	9.16	0.58
TL-13	1180.6	3.0	0.0268	0.71	556.4	59.7	1.20	0.23	12.11	0.29	15.45	0.56
WX-01	1305.3	1.2	0.0214	0.23	478.3	49.4	2.14	0.16	5.38	0.13	4.32	0.45
WX-02	1331.5	3.6	0.0478	0.65	512.5	54.5	1.65	0.19	4.21	0.25	5.51	0.57
WX-03	1349.9	4.3	0.0304	0.69	519.7	54.4	1.24	0.16	3.04	0.61	12.02	0.80
WX-04	1364.2	2.2	0.0120	0.43	513.3	42.2	2.63	0.29	19.27	0.30	20.31	0.51
WX-05	1398.2	2.8	0.0228	0.58	506.4	53.8	1.91	0.22	13.48	0.52	31.13	0.70
WX-06	1434.6	1.0	0.0204	0.19	536.9	36.2	–	–	–	–	–	–
ZQ-01	1468.2	2.2	0.0159	0.61	522.7	59.9	1.51	0.24	8.55	0.38	13.77	0.62
ZQ-02	1478.7	2.7	0.0188	0.48	495.2	42.9	1.60	0.27	17.45	0.34	21.72	0.56
ZQ-03	1482.6	0.7	0.0165	0.18	548.9	24.2	–	–	–	–	–	–
ZQ-04	1491.3	3.4	0.0322	1.00	526.8	95.5	1.92	0.25	5.97	0.42	10.16	0.63
ZQ-05	1498.9	11.7	0.0451	1.47	515.8	87.5	1.74	0.16	1.49	0.47	4.37	0.75
ZQ-06	1514.3	5.6	0.0266	0.72	497.5	60.5	2.01	0.21	4.34	0.24	5.85	0.53
ZQ-07	1528.3	7.9	0.0203	1.27	481.6	114.9	2.03	0.06	1.64	0.16	4.83	0.75
ZQ-08	1542.1	0.9	0.0388	0.13	561.3	17.9	–	–	–	–	–	–
ZQ-09	1580.5	2.3	0.0159	0.38	512.7	41.5	1.59	0.32	3.87	0.44	7.47	0.58

adsorption peaks for TYF coal-measure shale are identical with coal, indicating OM molecular structure and mineral composition in coal-measure shale are the same or closely similar to those of coal. With the increase of TOC, the peak area attributed to minerals gradually decreases, while that of OM increases.

The mineral absorption peaks of samples are mainly distributed in the following adsorption bands. The peaks located in the region of 480-520 cm^{-1} are overlapped absorption peaks for clay minerals, including illite, kaolinite, etc. Two small peaks at 780 and 800 cm^{-1} are attributed to quartz with an amorphous structure. A sharp band at 1100 cm^{-1} is the O-Si stretching vibration peak, also an overlapped adsorption band contributed to clay minerals, such as quartz, kaolinite and illite. The lower TOC the sample has, the sharper the band at 1100 cm^{-1} is. The peak observed at 3370 cm^{-1} arises from O-H vibration in kaolinite, two sharp bands located at 3700 cm^{-1} and 3620 cm^{-1} are due to kaolinite and illite (Pfeiferper and Avnir, 1983; Mastalerz et al., 2005; Wang et al., 2011; Li et

al., 2015).

The adsorption band for OM are mainly distributed in the following intervals: the band in the region (700-900 cm^{-1}) represents the out-of-plane deformation vibration of C-H in aromatic structure; the band in the region (1000-1800 cm^{-1}) mainly arises from oxygenated groups, and also contributes to C=C stretching vibration in aromatic structures and CH$_3$/CH$_2$ bending vibration; the aliphatic C-H stretching band between 2800 and 3000 cm^{-1} includes five spectral bands: symmetrical stretching vibration for CH$_2$ and CH$_3$ at 2850 cm^{-1} and 2865 cm^{-1}, asymmetrical stretching vibration for CH$_2$ and CH$_3$ at 2925 cm^{-1} and 2955 cm^{-1}, and stretching vibration for CH at 2890 cm^{-1}. The aromatic C-H stretching regions are observed at 3000-3100 cm^{-1} (Fig. 5) (Pfeiferper and Avnir, 1983; Li et al., 2015).

3.1.3 FTIR structure parameters

The macromolecules of OM in coal-measure shale have undergone a series of chemical changes during maturation,
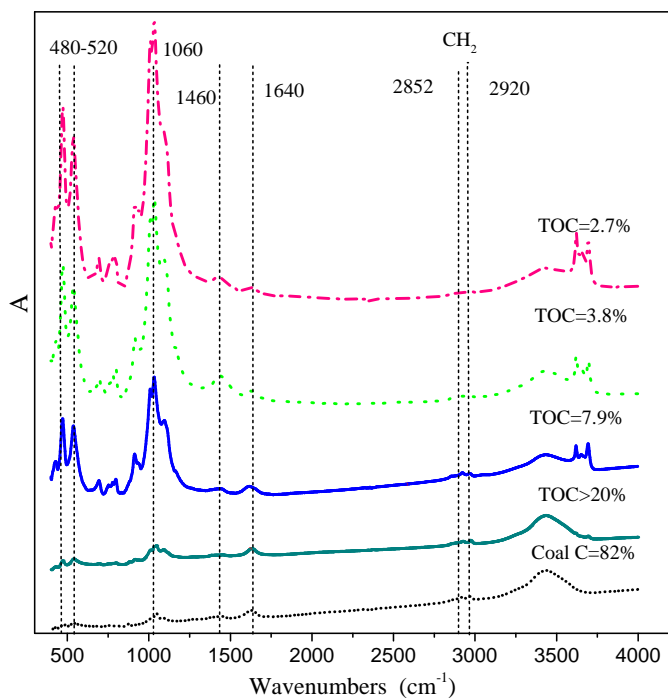
Fig. 4. FTIR spectra of shale and coal samples.

(a)

(b)

(c)
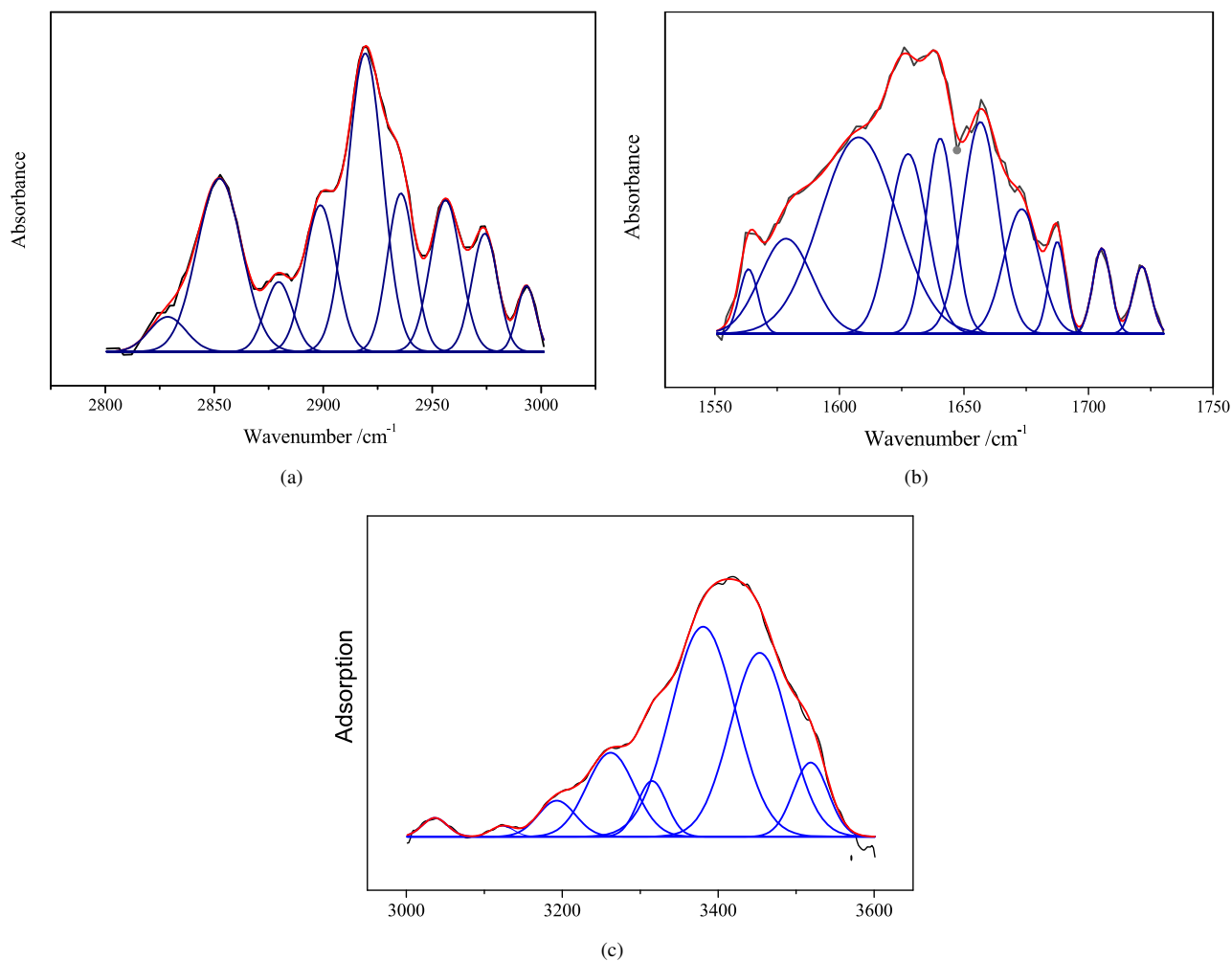
Fig. 5. An example of curve-fitting for the shale sample (TL-06).
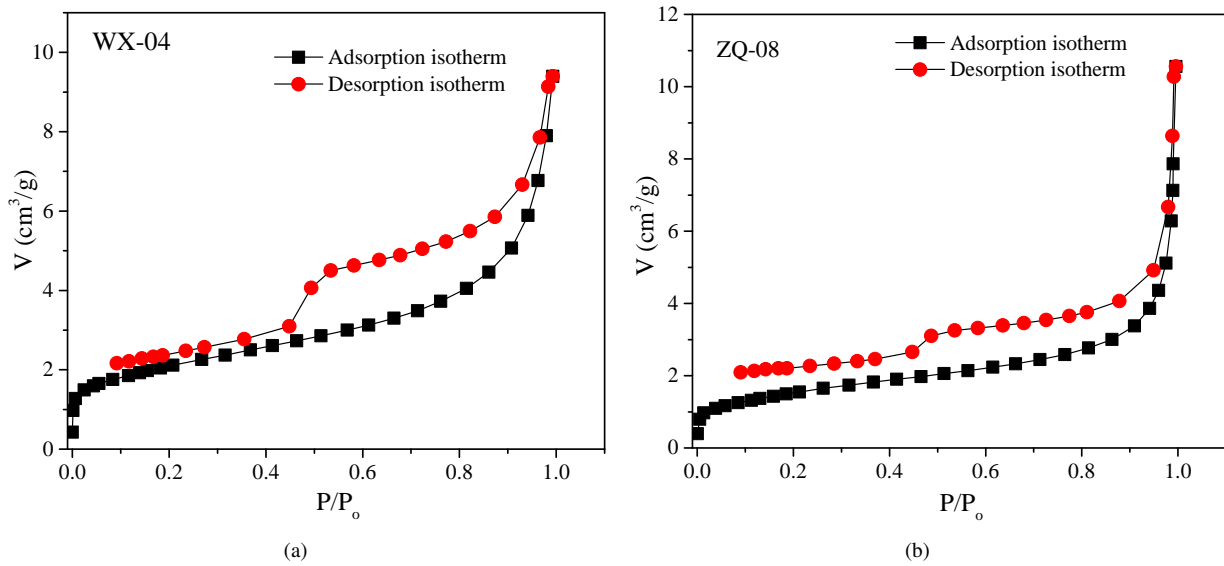
Fig. 6. N$_2$ adsorption-desorption isotherms for shale samples.

and the values of O/C and H/C also have an effect on the macromolecular structure of the OM. For the difference in maturation and kerogen composition, there are also differences in OM macromolecular structure. In order to quantitatively characterize the diversity of macromolecular structure, the following parameters were used. The position and area of each absorption peak is obtained by peak fitting (Fig. 5) (Pfeiferper and Avnir, 1983; Jaroniec and Avnir, 1989; Mastalerz et al., 2005; Wang et al., 2011; Li et al., 2015).

$$I_1 = \frac{CH_2}{CH_3} = \frac{A(2920)}{A(2950)} \tag{3}$$

the parameter I_1 was used to characterize the length of aliphatic chain and branching degree.

$$I_2 = \frac{A(3000 - 3100)}{A(2800 - 3000)} \tag{4}$$

$$I_3 = \frac{A(700 - 900)}{A(2800 - 3000)} \tag{5}$$

I_2 and I_3 are the ratio of aromatic carbon to aliphatic.

$$DOC_1 = \frac{A(2800 - 3000)}{A(1600)} \tag{6}$$

$$DOC_2 = \frac{A(700 - 900)}{A(1600)} \tag{7}$$

DOC are the parameters that describe the degree of aromatic carbon condensation. The band near 1600 cm^{-1} arises from aromatic C=C stretching vibration.

$$A = \frac{A(2800 - 3000)}{A[(2800 - 3000) + A(1600)]} \tag{8}$$

A is used to describe the hydrocarbon generation potential of OM in shale samples.

OM absorption peaks for the samples (TOC <1%) are weak and are seriously disturbed by mineral peaks. In this study, we did not calculate the FTIR structure parameters of the samples with TOC below 1%. There is only one sample with TOC over 20% which is special and isn't discussed either.

The results of FTIR parameters calculation by peak fitting for samples are shown in Table 1. I_1 varies from 1.20 to 2.63 with a mean value of 1.73, which is equivalent to the value of medium-high rank coal, indicating that OM in these shale samples is in the high-over maturity. The I_2 varies from 0.056 to 0.392, with an average of 0.21. Although the OM in the study area is in the high-over mature stage, the I_2 of shale samples is comparatively smaller. The parameter I_2 for coal with the same maturity is generally from 0.5 to 1. The value of DOC_1 varies from 0.13 to 0.91, and the average value is 0.37. The maturity of OM in shale samples is almost the same. Thus the differences of DOC_1 values are possibly due to distinct content of C=C in shale samples with different TOC. All samples have a very large DOC_2, from 4.32 to 39.12, which results from the adsorption band for minerals in 700-900 cm^{-1}. For the same reason, all samples have a large I_3 as well.

3.2 Lp-N$_2$GA adsorption/desorption

3.2.1 N$_2$ adsorption/desorption isotherm

Although the N$_2$ adsorption curves of samples have slight differences in morphology, they are all identified as type II adsorption isotherms according to IUPAC (IUPAC, 1994). The adsorption isotherm for shale samples can be divided into three intervals according to adsorption characteristics (Fig. 6). In the P/P_o range of 0-0.1, the adsorption curve is similar with Langmuir isotherm and monolayer adsorption occurs in the micropores (<2 nm). In the P/P_o segment between 0.1 and 0.8, the adsorption isotherm presents a steadily rising curve, indicating that mesopores (2-30 nm) are well developed. As the P/P_o becomes greater than 0.8, especially greater

Table 2. Pore structure parameters derived from N$_2$ adsorption (Unit: Pore volume (PoreV) cm^3/100g, Surface area (SurA) m^2/g).

Samples	BET SurA	BJH PoreV	BJH PoreV (<10 nm)	BJH PoreV (<20 nm)	BJH PoreV (<50 nm)	Micro PoreV	Average PoreW (nm)
TL-01	5.6	1.2	0.61	0.72	1.01	0.24	8.9
TL-02	9.5	1.2	0.38	0.64	0.88	0.51	6.4
TL-03	11.1	1.8	0.89	1.12	1.40	0.51	6.4
TL-04	2.1	1.5	0.31	0.44	0.60	0.11	26.9
TL-05	5.7	1.2	0.33	0.56	0.70	0.28	9.2
TL-06	15.3	3.0	1.56	1.79	2.17	0.65	5.7
TL-07	12.1	2.0	0.86	1.17	1.45	0.58	7.4
TL-08	8.0	1.4	0.69	0.86	1.02	0.37	7.5
TL-09	6.2	1.0	0.35	0.53	0.71	0.28	6.4
TL-10	16.3	3.3	1.78	2.31	2.40	0.78	5.9
TL-11	9.9	2.1	1.04	1.23	1.68	0.44	8.8
TL-12	11.1	1.9	0.57	0.80	1.43	0.54	6.8
TL-13	12.0	2.7	1.22	1.53	1.88	0.50	9.6
WX-01	5.7	1.8	0.27	0.46	0.91	0.25	12.9
WX-02	13.5	2.8	1.23	1.92	2.25	0.56	11.7
WX-03	15.4	3.1	1.47	1.87	2.32	0.63	6.8
WX-04	8.0	1.4	0.69	0.92	1.32	0.33	7.8
WX-05	10.7	2.2	0.72	1.10	1.35	0.46	8.6
WX-06	4.7	1.5	0.39	0.62	0.83	0.21	10.1
ZQ-01	9.6	2.8	0.77	0.87	1.09	0.40	9.9
ZQ-02	9.3	2.2	1.01	1.27	1.68	0.37	8.5
ZQ-03	1.4	0.7	0.14	0.25	0.47	0.08	20.9
ZQ-04	13.2	2.1	1.13	1.37	1.83	0.59	6.7
ZQ-05	17.4	2.9	1.94	2.14	2.37	0.77	6.0
ZQ-06	15.5	2.4	1.24	2.03	2.21	0.65	6.7
ZQ-07	10.5	2.2	1.64	1.78	1.93	0.69	7.2
ZQ-08	5.6	1.5	0.32	0.43	0.81	0.31	11.9
ZQ-09	8.5	2.0	0.68	0.85	1.19	0.37	9.9

than 0.9, the adsorption isotherm increases steeply and the multilayer adsorption occurs in mesopores (about 30-50 nm) and macropores (about 50-300 nm) (Zhang et al., 2016; Ko et al., 2017; Shao et al., 2017; Kong et al., 2019; Liu et al., 2019).

The hysteresis loop of shale samples is between H$_2$ and H$_3$ with most samples closer to H$_3$, which indicates that the slit type and ink bottle type pores are developed, with slit type pores predominating (IUPAC, 1994).

3.2.2 Pore structure parameters and pore size distribution (PSD)

The pore structure parameters derived from the N$_2$ adsorption isotherm are shown in Table 2. The BET surface area varies from 1.4 to 17.4 m^2/g, with an average of 9.8 m^2/g. The BJH pore volume is 0.7 and 3.3 m^3/100g. It is noticeable that the average value of pore volume (<20 nm) accounts for more than 50% of the total BJH pore volume, indicating pores less than 20 nm are well developed. The pore size is mainly

distributed between 5.7 and 26.7 nm, with an average size of 9.3 nm.

The PSD obtained from N$_2$ adsorption data shows that the pore size covers a wide range (Fig. 7) from several nanometers to hundreds nanometers. The highest peak of most samples is around 2 nm; a lower peak is around 2-3.5 nm, and most pores are smaller than 4 nm. In some samples (Eg: TL-10, WX-03 and ZQ-06), pores between 10-30 nm are well developed, probably because these samples are rich in pyrite and siderite.

3.3 OM-related pores in FE-SEM images

OM plays a vital role in controlling the development and evolution of micro-nanometer pores in shale. OM hydrocarbon generation and expulsion, OM acid erosion and mutual support among OM can all promote pore development in shale (Edgar and Rafael, 1996; Curtis et al., 2012; Yang et al., 2016; Shao et al., 2017). In our work, the OM-related pores are divided into the following types: OM hydrocarbon-generating pores,
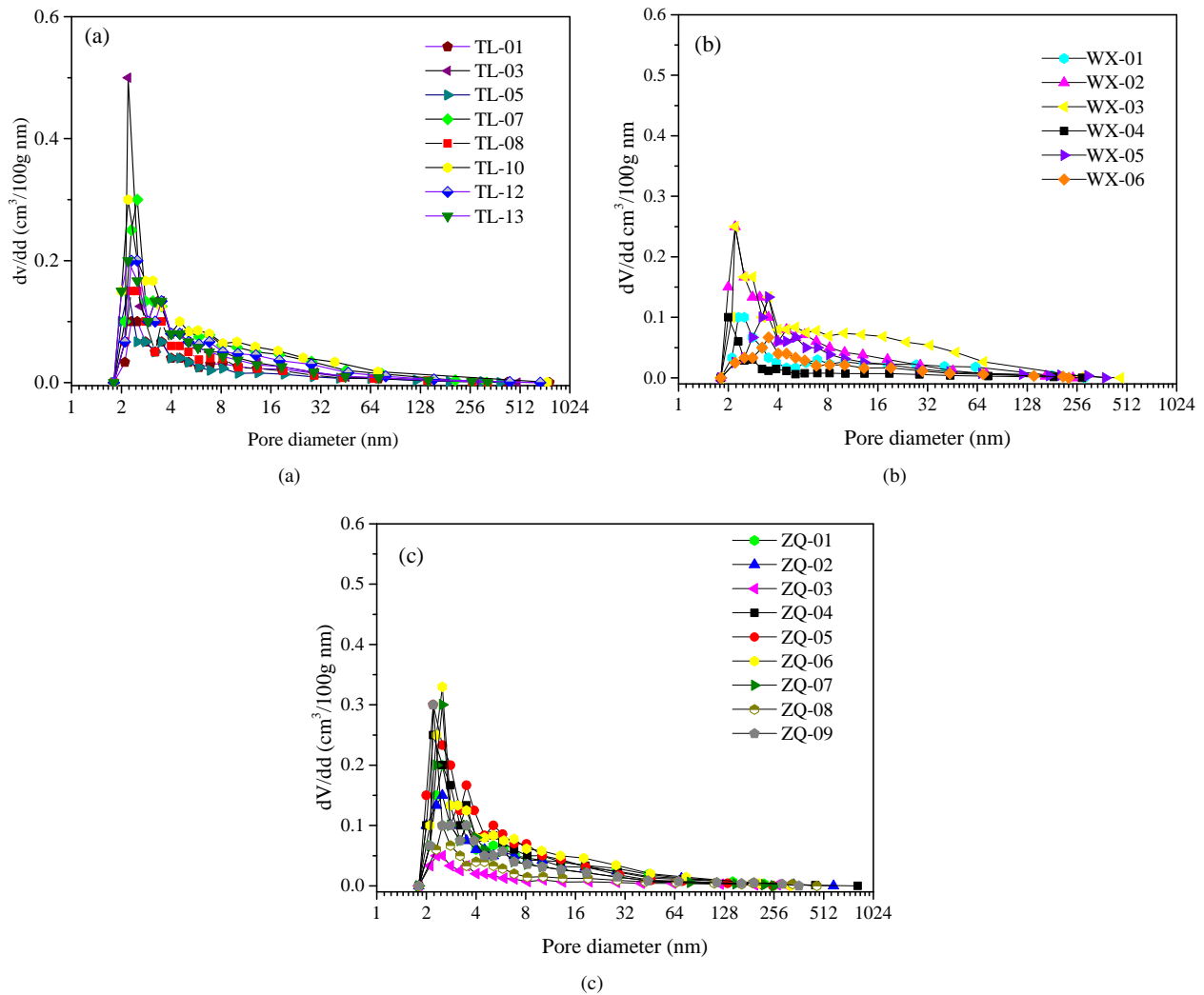
Fig. 7. PSD derived from N$_2$ adsorption branches with the BJH model.

OM intergranular pores, OM structural pores and OM-related micro-cracks.

There are two main forms for OM in TYF shale samples observed by FE-SEM (Figs. 8a and 8b). One is flakes on the mineral grains; the other is particles filled in the minerals.

3.3.1 OM hydrocarbon-generating pore

The OM hydrocarbon-generating pores are caused by generation of light hydrocarbon and inorganic gases after the OM maturity reaches the "oil window". Most of them are scattered in OM enriched regions (Fig. 8). Some are surrounded by nanometer cracks, which is favorable to improve the connectivity of OM pores. The OM hydrocarbon-generating pores have a wide size range, from several nanometers to hundreds micrometers and most of them are less than 10 nm (Figs. 8c-8h). Those pores present various morphologies, such as circle, ellipse, triangle, irregular (Figs. 8g and 8h), etc. Generally speaking, the nanometer pores are more developed in samples with high TOC (Figs. 8c-8f). In the samples with smaller TOC, the micrometer pores are less developed, mostly isolated and scattered on the surface of OM (Figs. 8i and 8j).

3.3.2 OM structural pores

Similar to coal, OM of coal-measure shale mainly originates from higher plants, and the macerals are mainly composed of vitrinite and inertinite with a small amount of liptinite. Some OM, mostly in the filament, remains the original pore of plants observed by FE-SEM (Fig. 8k: TL-03). A large number of micrometer short-cracks were developed on the surface of OM in some samples (Fig. 8l: TL-10). Some researchers believe that such cracks are caused by the shrinkage of OM due to gold coating treatment. However, all samples need to be gold-coated before FE-SEM identification. This is only observed in a very small number of samples. Therefore, whether the gold coating has enough effect to cause the shrinkage of OM needs further exploration. Those short cracks discovered in inertinite may be the residual structure of lignocelluloses cells in silk carbonization in higher plants.

3.3.3 OM intergranular pores

Some intergranular pores are found among OM particles or between OM and mineral particles. Controlled by the mor-

(a)　　　　　　　　　　　　　　　　　(b)

(c)　　　　　　　　　　　　　　　　　(d)

(e)　　　　　　　　　　　　　　　　　(f)

(g)

(h)

(i)

(j)

(k)

(l)
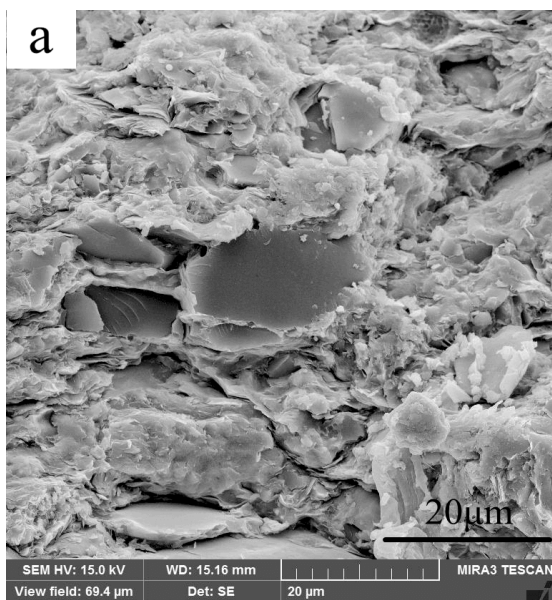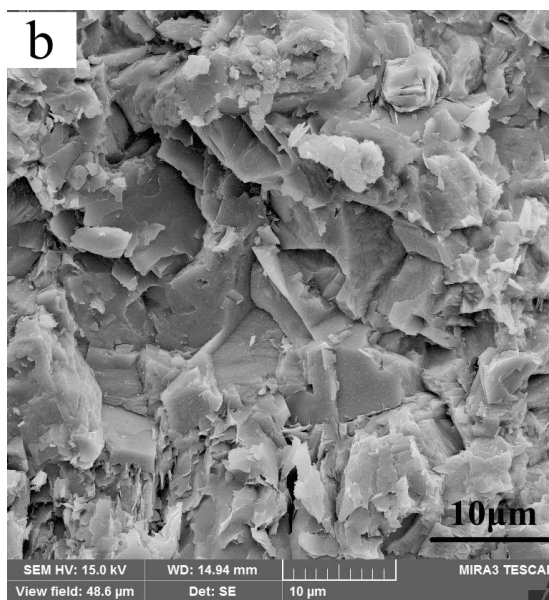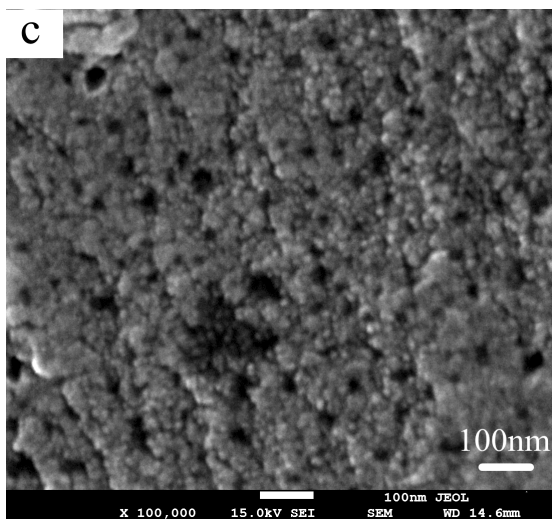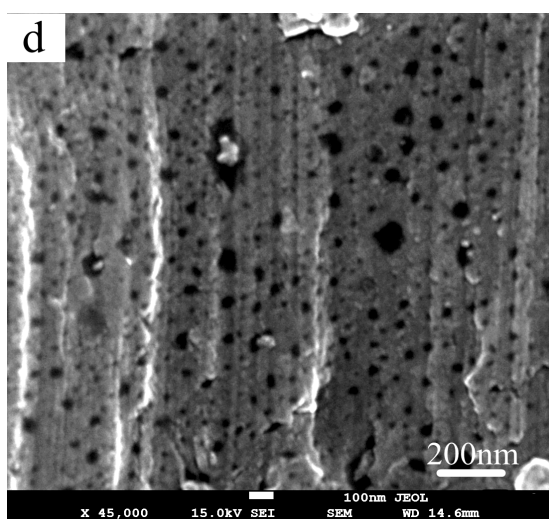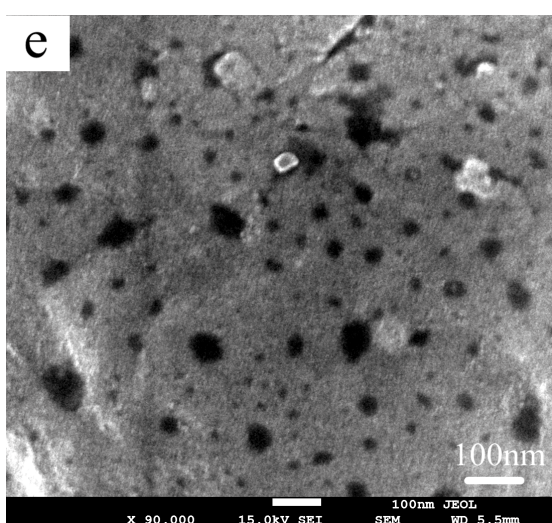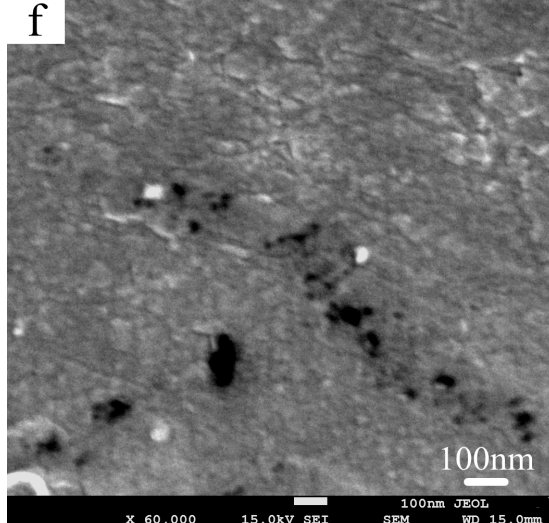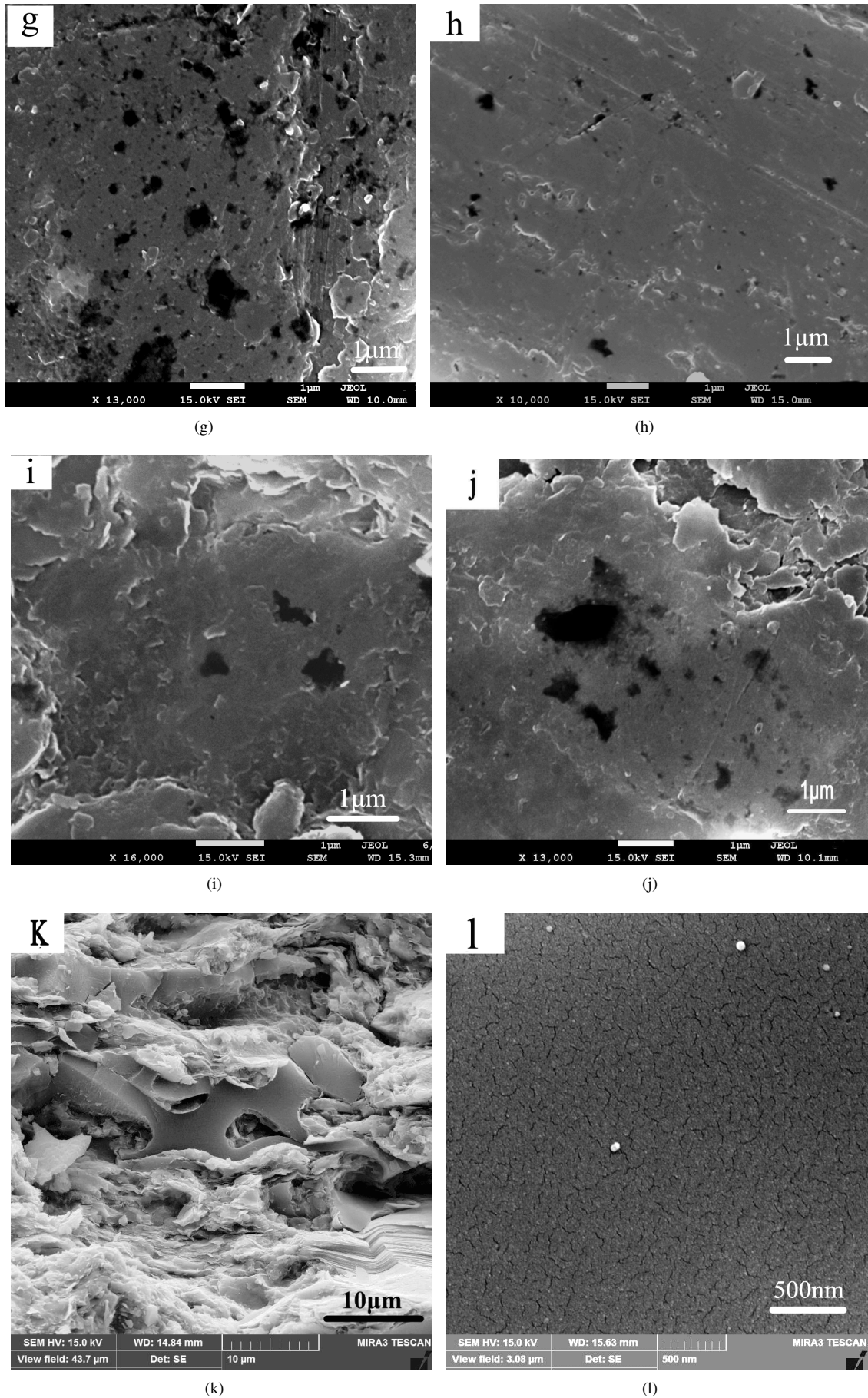
Fig. 8. (a) (b): flaky and detrital OM (a: TL-03, b: WX-04); (c)-(f) nanometer OM pores (c, d: ZQ-05; e, f: ZQ-07); (g)-(j): micrometer OM pores (g: TL-06, h: WX-02, i: TL-11, j: TL-01); (k): OM structure pore (TL-03); (l): a large number of short fractures without pores on the OM (TL-10).

(a)

(b)
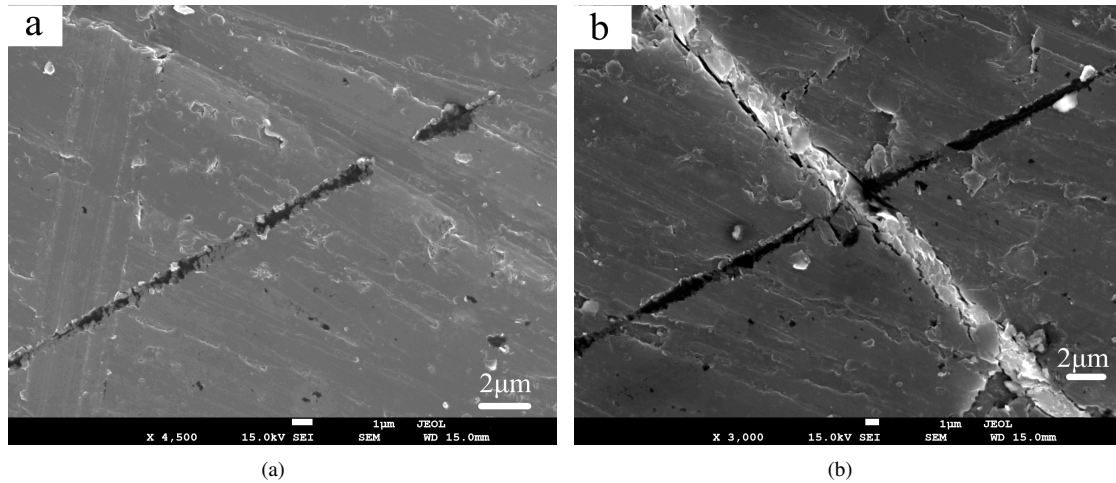
Fig. 9. Micron-scale fracture on OM (WX-03, TL-07).

phology of mineral particles, these pores are mostly irregular in shape, with sizes ranging from several microns to hundreds microns (Figs. 8a and 8b).

3.3.4 Micro-fractures in OM

Micro-fractures on the surface of OM can reach tens of microns in length. It may be caused by shear stress rupture or contraction of OM hydrocarbon generation (Figs. 9a and 9b).

3.3.5 Intergranular pores of pyrite around OM

OM plays an important role in the formation of pyrite, which indirectly affects the development of intergranular pores in pyrite. Fig. 10 indicates that pyrite crystals coexist with OM in most cases. The granular pyrite crystals are directly in contact with OM, while nest-like pyrite crystals are covered with OM.

The formation of pyrite in coal measure strata requires not only a medium-low oxygen-poor sedimentary environment,

but also an appropriate supply of iron, OM and anaerobic bacteria. It is believed that the aggregation of nest-like pyrite crystals is the result of nodules and growth for iron in space restricted by OM. Around OM, a large number of intergranular pores are developed among the crystals with various morphologies in a submicron-size scale.

3.4 Pore fractal dimensions from N_2 Adsorption Isotherms

In this study, the FHH model was used to calculate the pore fractal dimension from N_2 adsorption data. Fig. 11 shows that there are two different linear lines in the P/P_o ranges of 0-0.45 and 0.45-1. The fitting coefficient R^2 of two segments for samples are all greater than 0.97, which suggests the different fractal features at two intervals. Two fractal dimensions D_1 and D_2 were obtained and they could be used to characterize roughness of pore surface and complexity of pore structure, respectively. Moreover, the pore size is about 4 nm at the

(a)

(b)
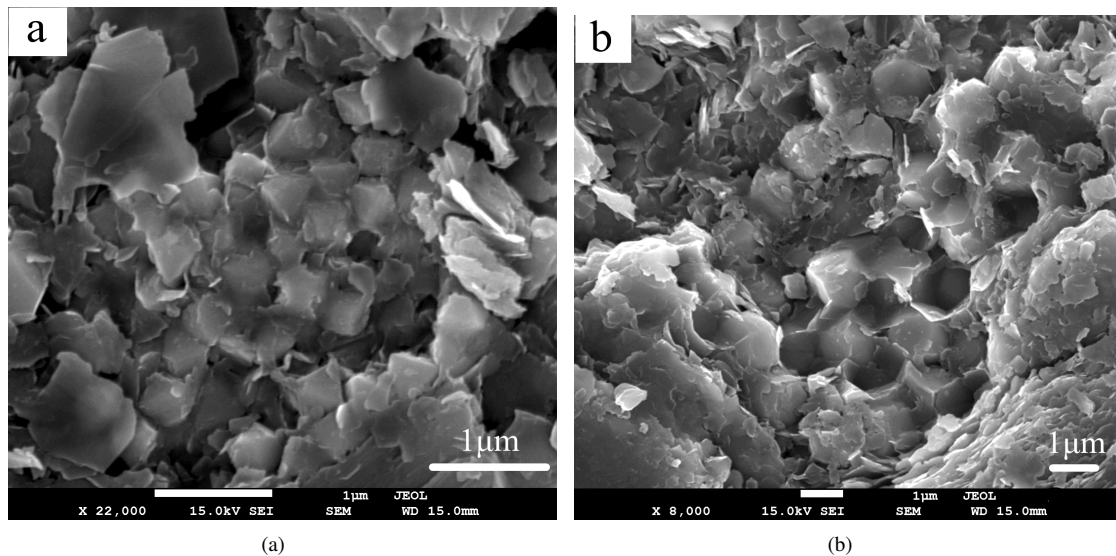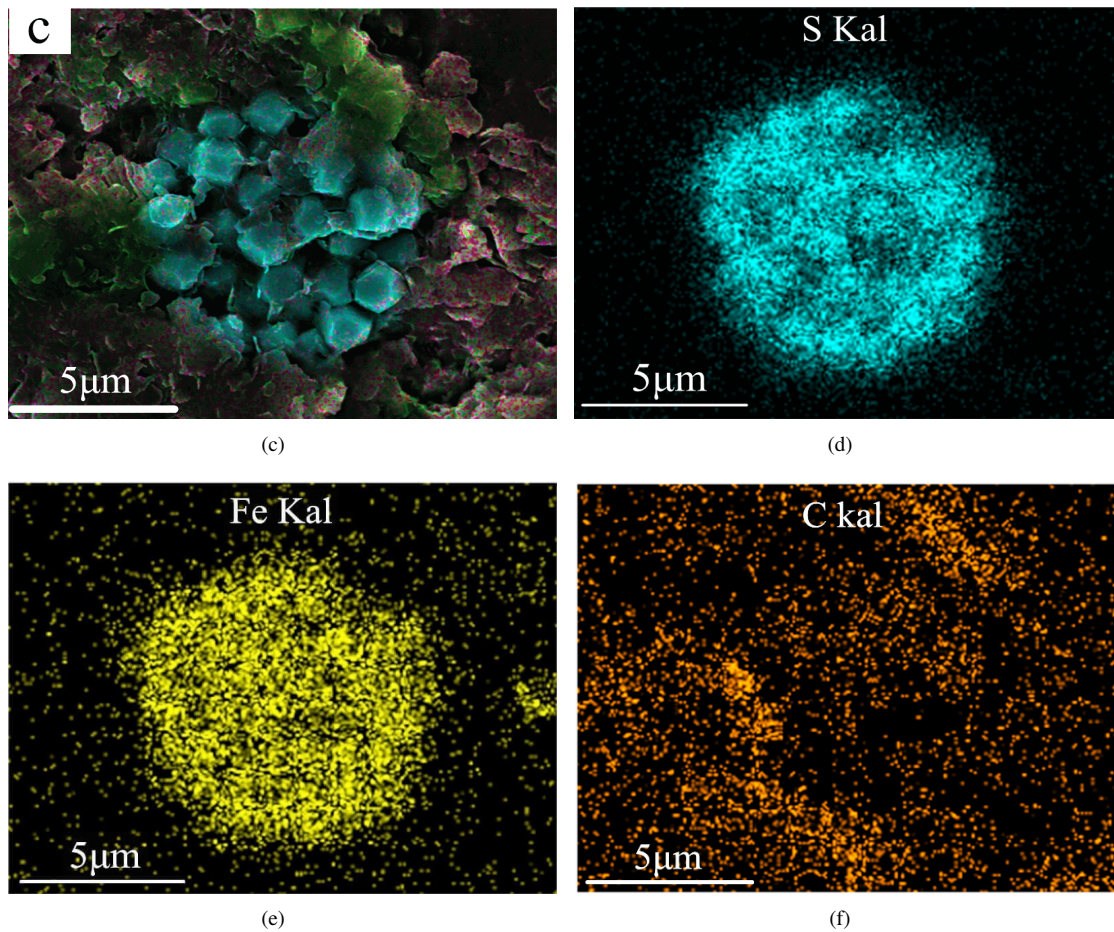
Fig. 10. Intergranular pores of pyrite around OM.

(a)

(b)
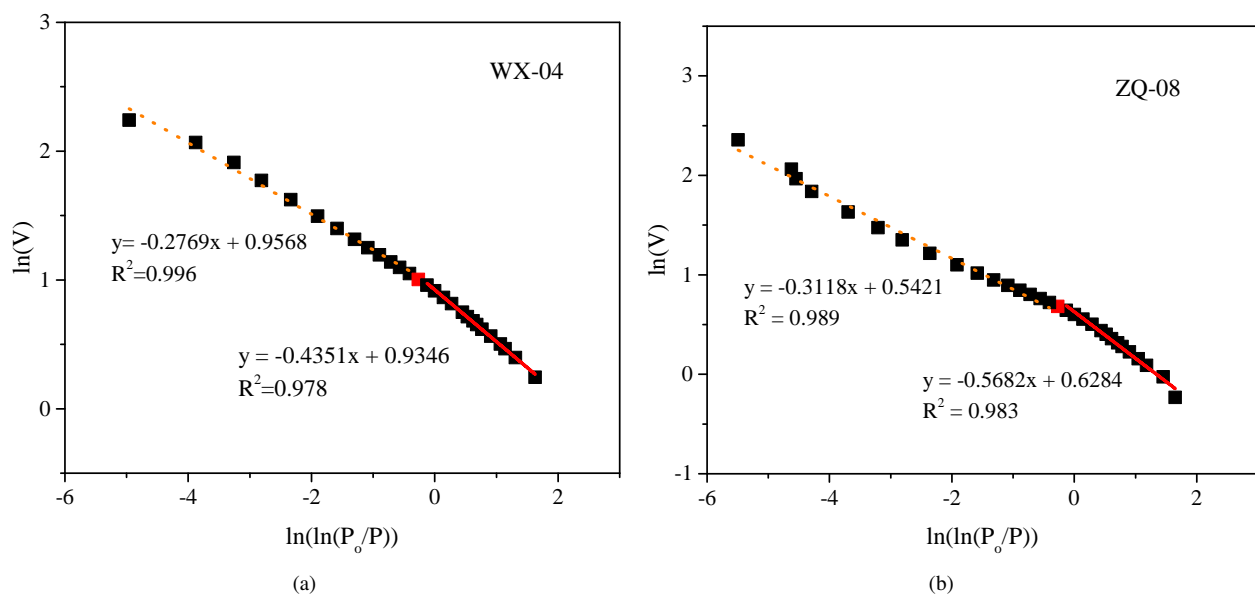
Fig. 11. Plot of ln(V) Vs. ln(ln(P$_o$/P)) reconstructed from the N$_2$ adsorption isotherms.

Table 3. Pore fractal dimensions based on FHH model.

Samples	$0<P/P_o<0.5$			$0.5<P/P_o<1$		
	K	D_1	R^2	K	D_2	R^2
TL-01	-0.586	2.414	0.98	-0.267	2.733	0.94
TL-02	-0.475	2.525	0.93	-0.214	2.786	0.99
TL-03	-0.465	2.535	0.95	-0.213	2.787	0.96
TL-04	-0.726	2.274	0.99	-0.428	2.572	0.97
TL-05	-0.575	2.425	0.95	-0.285	2.715	0.99
TL-06	-0.399	2.601	0.98	-0.266	2.734	0.99
TL-07	-0.476	2.524	0.95	-0.244	2.756	0.99
TL-08	-0.603	2.397	0.98	-0.245	2.755	0.99
TL-09	-0.616	2.384	0.97	-0.245	2.755	0.99
TL-10	-0.405	2.595	0.94	-0.213	2.787	0.99
TL-11	-0.452	2.548	0.98	-0.276	2.724	0.97
TL-12	-0.466	2.534	0.96	-0.231	2.769	0.99
TL-13	-0.509	2.491	0.95	-0.278	2.722	0.98
WX-02	-0.692	2.308	0.97	-0.398	2.602	0.99
WX-03	-0.469	2.531	0.99	-0.358	2.642	0.96
WX-05	-0.437	2.563	0.99	-0.255	2.745	0.98
WX-07	-0.435	2.565	0.98	-0.277	2.723	0.99
WX-09	-0.423	2.577	0.98	-0.262	2.738	0.99
WX-11	-0.524	2.476	0.99	-0.299	2.701	0.98
ZQ-01	-0.484	2.516	0.97	-0.344	2.656	0.99
ZQ-03	-0.497	2.503	0.97	-0.284	2.716	0.97
ZQ-05	-0.728	2.272	0.99	-0.439	2.561	0.99
ZQ-07	-0.400	2.600	0.96	-0.210	2.790	0.94
ZQ-09	-0.383	2.617	0.99	-0.201	2.799	0.99
ZQ-11	-0.438	2.562	0.97	-0.278	2.722	0.99
ZQ-13	-0.440	2.560	0.99	-0.231	2.769	0.99
ZQ-15	-0.568	2.432	0.98	-0.312	2.688	0.99
ZQ-17	-0.435	2.565	0.97	-0.292	2.708	0.99

P/P_o of 0.45 based on N_2 adsorption data. The pores could be divided into small pores and large pores with 4 nm as the demarcation point, and D_1 and D_2 can also be used to describe the pore structure of small pore and large pore. D_1 is from 2.272 to 2.617, and D_2 is between 2.561 and 2.799, D_2 is larger than D_1 (Table 3).

4. Discussion

In order to explore the influence of OM macromolecular structure on pore structure and fractal characteristics, the relationships between the measured parameters are considered.

4.1 Relationships between FTIR parameters and Rock-eval parameters

The relations between FTIR parameters and T_{max} are shown in Fig. 12. A weak negative correlation was observed between T_{max} and I_1, while a weak positive correlation was observed

between T_{max} and DOC_1 for most samples (Fig. 12c Area A). The larger the I_1 is, the greater the branching degree and the higher the components with poor thermal stability are, such as aliphatic chains and functional groups, resulting in a lower T_{max}. Correspondingly, as the DOC value increases, the branching degree decreases, while the aromatic carbon content, the size of aromatic nuclei and the components with good thermal stability increase, resulting in a greater T_{max}.

4.2 Relationships between FTIR parameters and pore fractal dimensions

From Fig. 13, the D_1 has a weak positive correlation with I_1. For samples with the same TOC, a larger I_1 implies longer aliphatic chains and greater branching degree of the OM. This is more favorable for precipitation of hydrocarbons and inorganic gases, leading to more nanometer OM hydrocarbon pores. I_1 is a dimensionless ratio parameter. Some samples
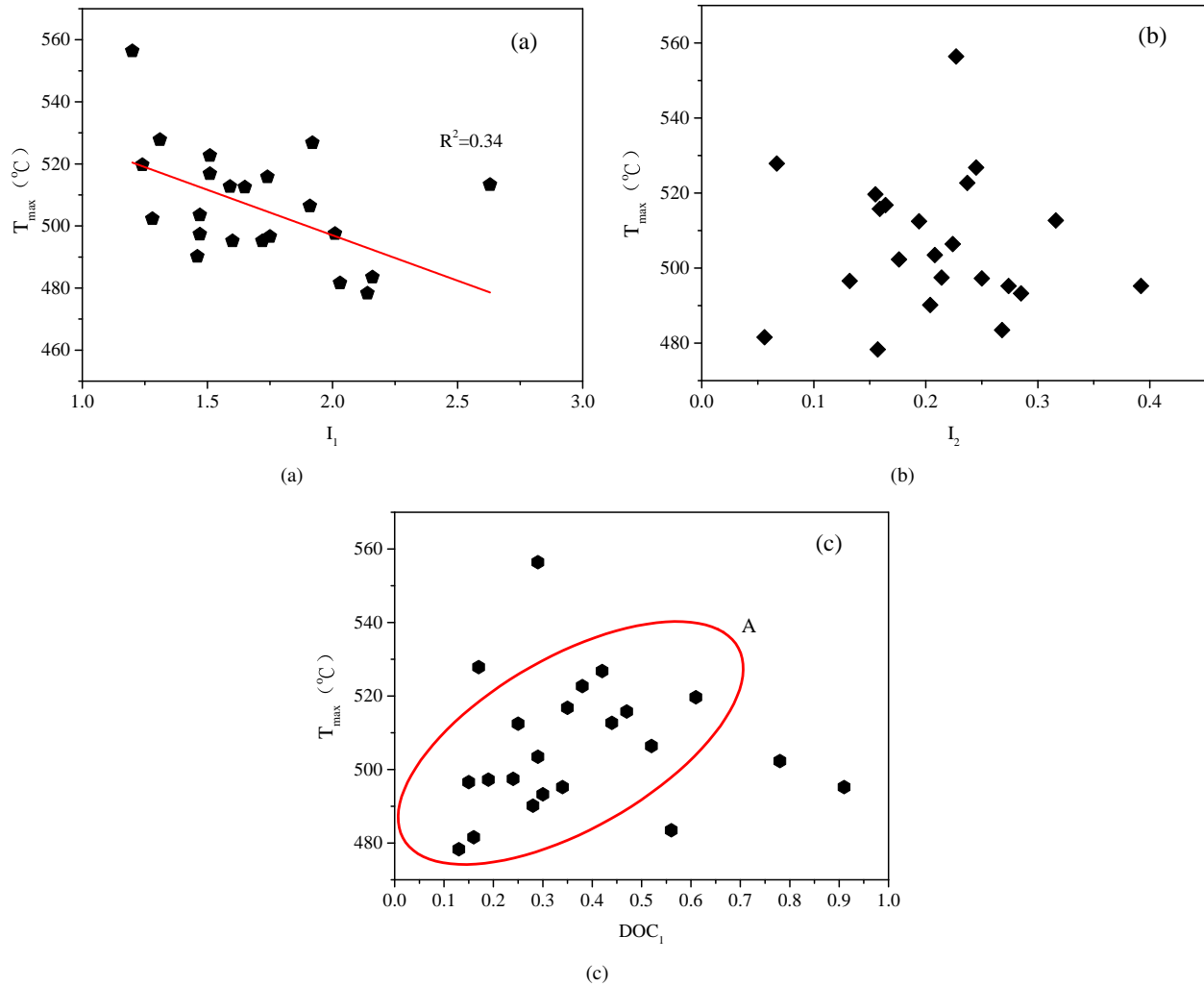
Fig. 12. Relationships between FTIR structure parameters and T_{max}.
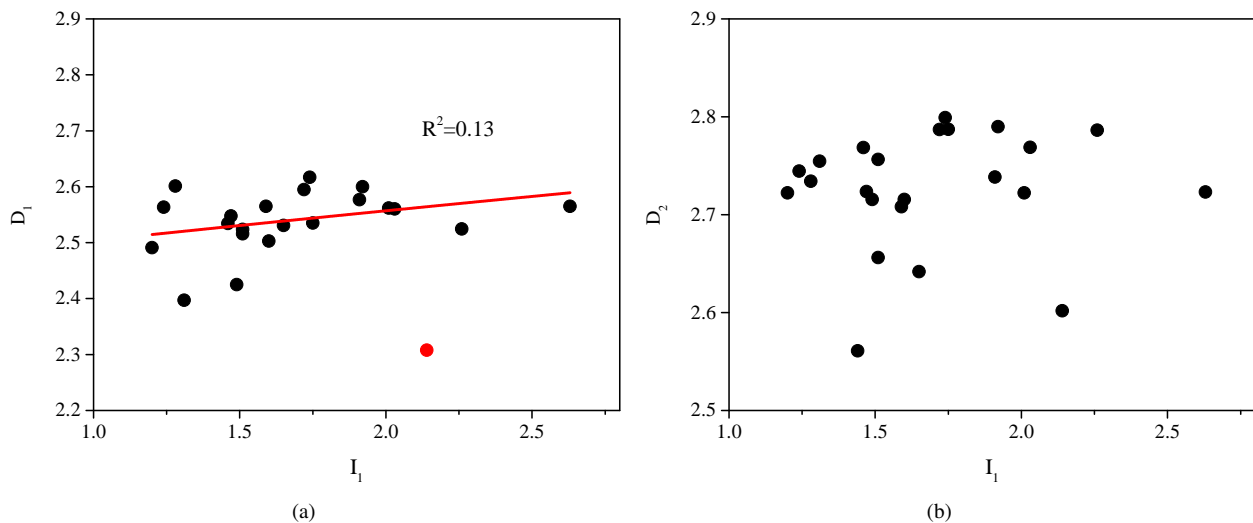
Fig. 13. Relationships between I_1 and pore fractal dimensions.
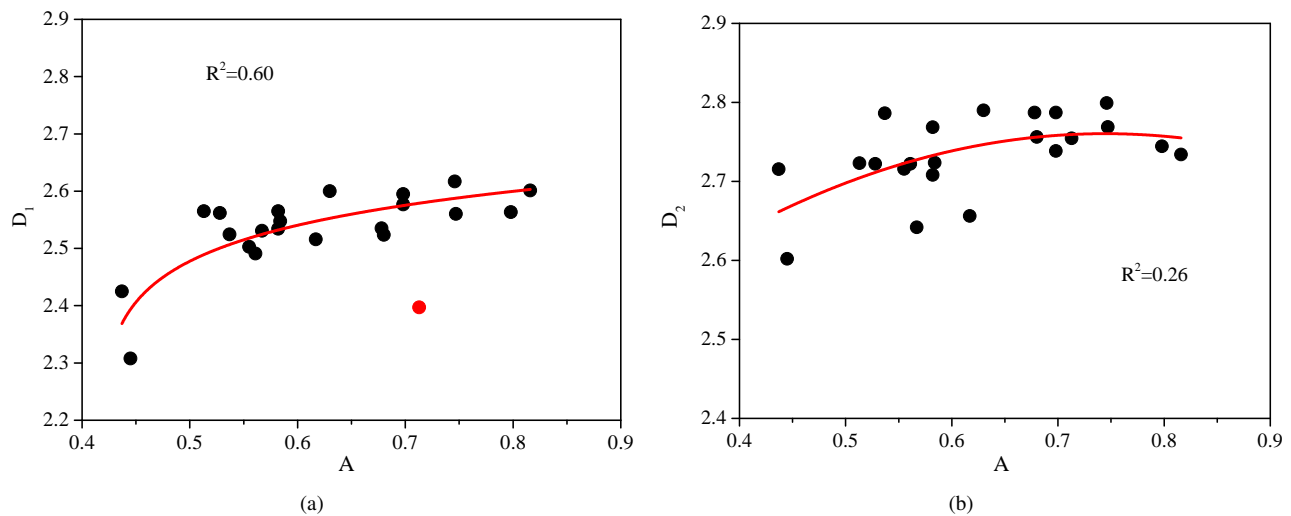
Fig. 14. Relationships between A and pore fractal dimensions.
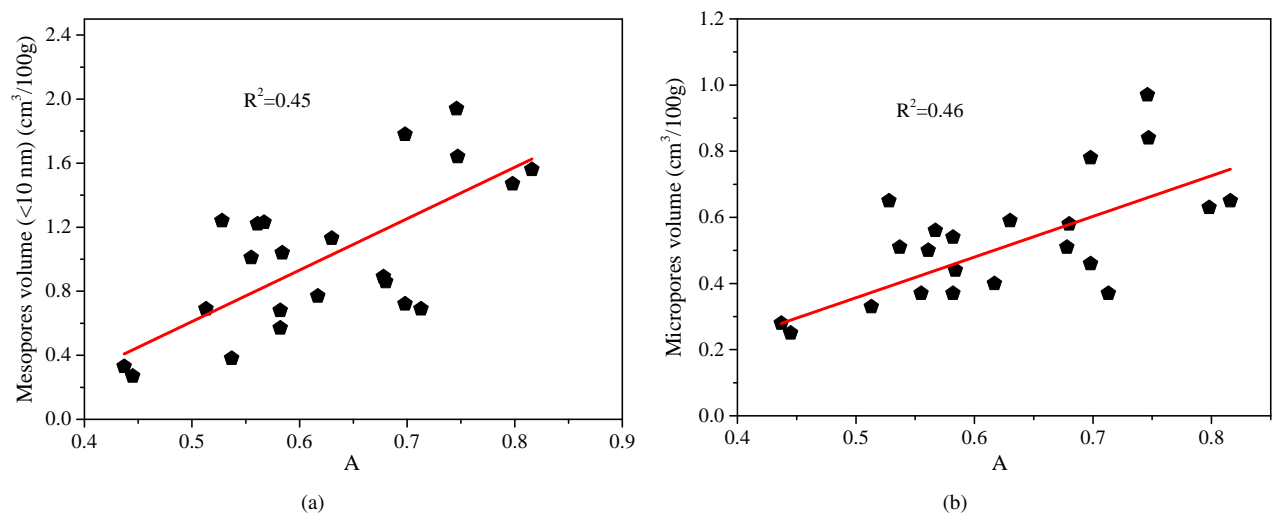
Fig. 15. Relationships between A and micro, mesopores (<10 nm) volume.

with a lower TOC (sample WX-01) though have a larger I_1, the total amount of aliphatic chains is lower and OM pores were less developed, leading to a smaller D_1 (Yang et al., 2014).

As Fig. 14 shows, D_1 has a logarithmic increasing functional relationship with A, whereas the relationship between D_2 and A is ambiguous. Both micropores and mesopores volume (<10 nm) have a moderate positive correlation with A (R^2 are 0.45 and 0.46, respectively) (Fig. 15). The relationship between A and D_2 is not clear, which is possibly due to the fact that OM hydrocarbon generation is more beneficial to the development of micropores and mesopores (<10 nm), while it has a smaller contribution to development of macropores and mesopores (>10 nm). These correlations indicate that the larger the value of A is, the more developed the micropores and mesopores (<10 nm) will be, resulting in a larger D_1 (Yang et al., 2014; Li et al., 2019).

From Fig. 16, a moderate positive linear relationship (R^2=0.41) between D_1 and DOC_1 is observed. For most

samples, D_2 has a very weak positive trend with DOC_1. Both microspores and mesopores (<10 nm) volume have a logarithmic incremental function with DOC_1 (R^2 are 0.47 and 0.53, respectively). For a few samples with higher TOC, though the DOC_1 is relatively smaller (ZQ-05, ZQ-07), the micropores are well developed, this may be due to the greater content of the aromatic carbon.

In the thermal evolution, aromatic nuclei of OM macromolecules in shale condensed gradually and the size was continuously growing by the combined effect of temperature and pressure. This may lead to a considerable amount of nanometer pores within aromatic structures or between aromatic nuclei and mineral particles. According to Figs. 13-17, it can be inferred that the pores formed by condensation of macromolecules are mainly micorpores and mesopore (<10 nm), with mesopores (<10 nm) being dominant. Combined with the pore size distribution (Fig. 7), such pores are mainly likely to be concentrated between 2-4 nm.

(a)

(b)
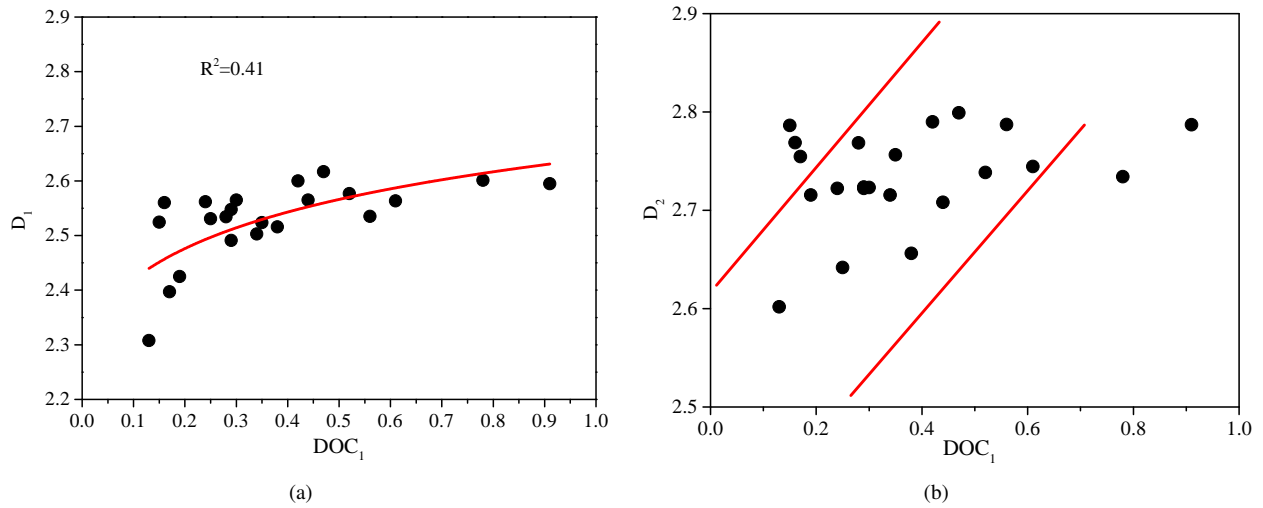
Fig. 16. Relationships between DOC_1 and pore fractal dimensions.

(a)

(b)
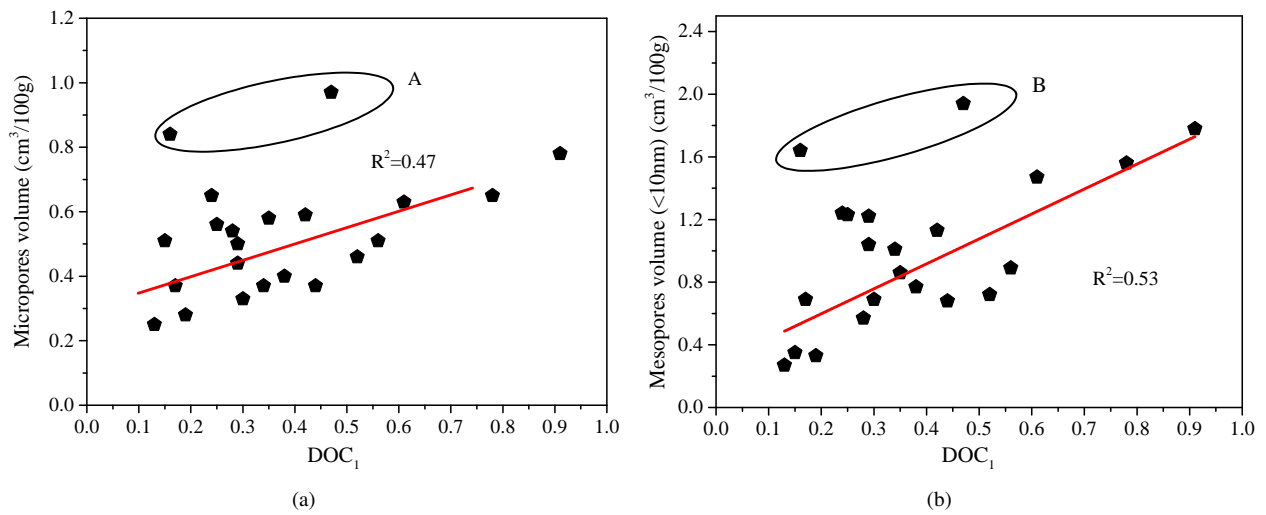
Fig. 17. Relationships between DOC_1 and micropores, mesopores (<10 nm) volume.

(a)

(b)
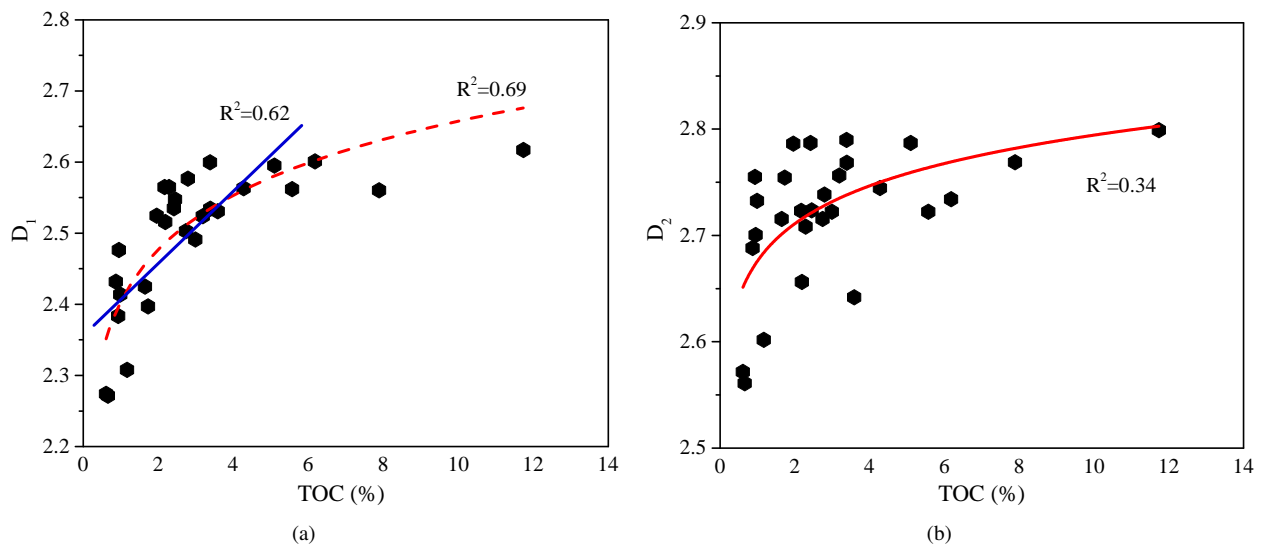
Fig. 18. The relationship between TOC and pore fractal dimensions.
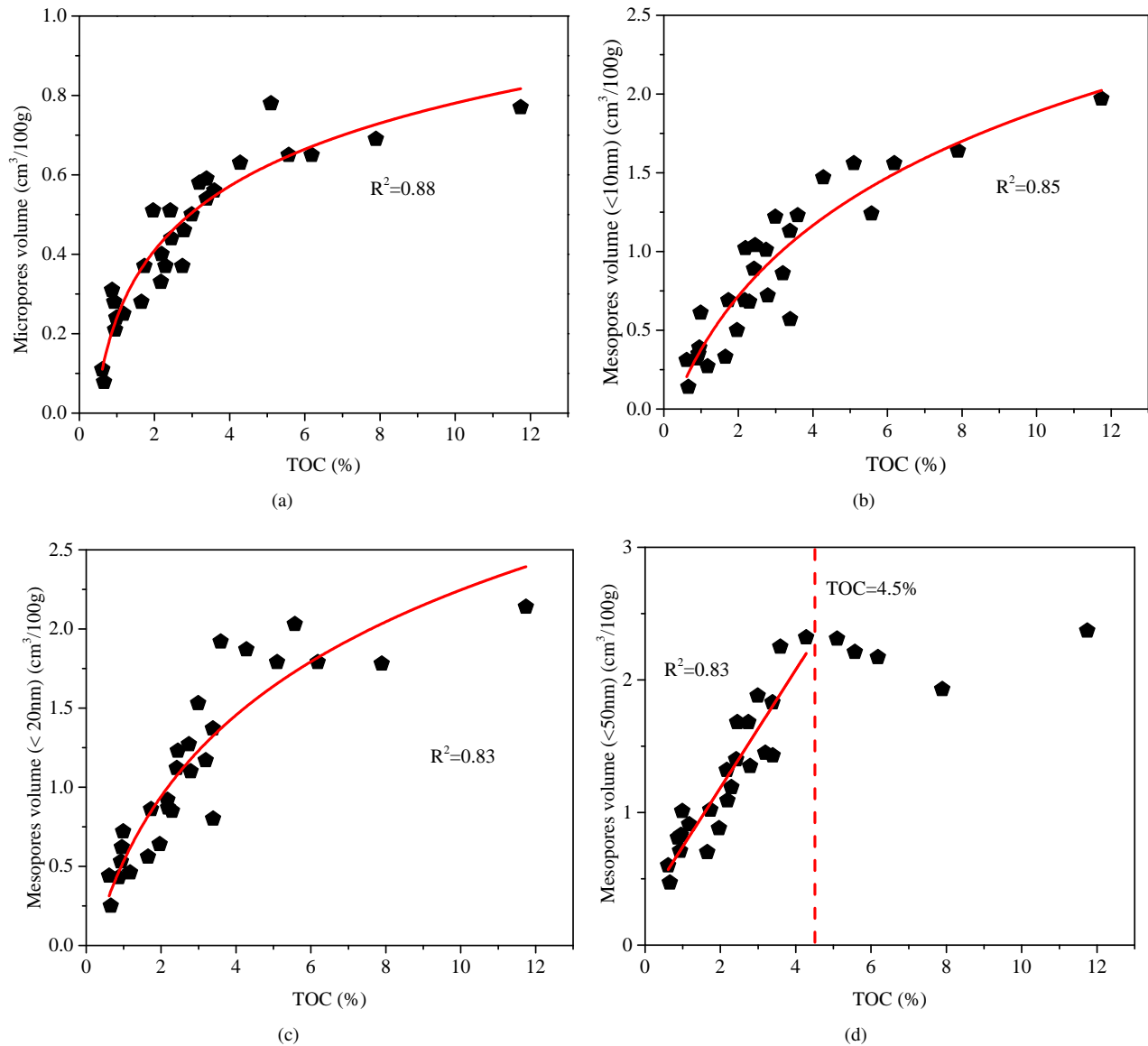
Fig. 19. Plots of TOC vs. pore volume with different size.

4.3 The relationships between OM macromolecular structure and pore fractal characteristics

As Fig. 18 shows, both D_1 and D_2 have a logarithmic increasing function with TOC. The increasing function relationship between D_1 and TOC is more obvious than that between D_2 and TOC. For the samples with TOC less than 6%, TOC has a good positive correlation with D_1.

By macroscopic observation and polarizing microscope analysis, it is found that OM is unevenly distributed in shale. For the dark grey shale sample with low TOC, OM is scattered in shale with a small continuous area. As the TOC increases, the color of the shale gradually changes from dark gray to grey-black, the OM distribution density and OM area increase (Fig. 2). As the TOC increases further, the color of shale turns to black, small OM regions are interconnected and form large area accumulations. This is particularly evident in

carbonaceous mudstones (Li et al., 2018a, 2019; Sheng et al., 2019).

It can be seen from Fig. 19 that BJH pore volumes with different sizes all have an increasing logarithmic functional relationship with TOC. Among them, the incremental function relation between TOC and pore volume of micropores as well as mesopores (<10 nm) are more obvious than others, which suggests high TOC is beneficial to the development of pores, especially micropores and mesopores less than 10 nm. This finding is consistent with the results of the FE-SEM observations. Compared with coal, the coal-measure shale has a smaller TOC no more than 20%, which leads to less amount of hydrogen-generation with small molecular mass, such as CH_4, CO_2 etc. Therefore, the size of OM hydrogen-generation pores is generally small. Meanwhile, the effect of aromatic condensation on pore development is also limited and will not lead to a large-scale shrinkage to produce macro-cracks or

cleats in OM as it does in coal.

As discussed above, a high value of TOC is very useful for the development of micropores and mesopores ($<$10 nm), so both D_1 and D_2 displays an incremental functional relation with TOC. The PSD (Fig. 7) indicates that pore size of shale samples is mainly concentrated in the range of 2-4 nm. For this reason the increasing functional relationship between TOC and D_1 is more obvious.

5. Conclusion

In this work, an integrated methodology was used to characterize the microscopic pore structure in coal-measure shale with different TOC by LpN$_2$GA, FE-SEM, FTIR and FHH methods. The primary conclusions are summarized as follows.

The TOC for all shale samples varies from 0.7% to 11.7% with a mean value of 3.1%. The kerogen is humic (type III) and the macromolecules of OM in coal-measure shale is similar to coal. The OM of the shale samples is in the phase of high-post maturity with T_{max} from 469.3 to 569.3 °C.

The pore size covers a wide range from several nanometers to hundreds of micrometers. However, the pores in the range of 0-20 nm are well developed and the average pore size is 9.3 nm. According to FE-SEM oberservation, OM related pores can be divided into following types: hydrocarbon-generating pores, intergranular pores, structural pores and micro-cracks. The hydrocarbon-generating pores less than 10 nm are the best developed. Two different pore fractal dimensions are obtained from the N$_2$ adsorption data with the FHH model in the range of 2.272-2.617 and 2.561-2.799, respectively.

The distribution of OM in coal-measure shale is heterogeneous. The larger the TOC and the more uniform the distribution of OM, the more micropores and mesopores ($<$10 nm) are developed in the shale, the larger the pore fractal dimension.

The larger the I_1 is, the more components with poor thermal stability in OM, leading to a smaller T_{max}. On the contrary, the larger DOC_1, the more components with high thermal stability in OM, resulting in a greater T_{max}. Both OM hydrocarbon-generation and condensation of aromatic nuclei play an important role in development of micropores and mesopores ($<$10 nm).

Acknowledgements

Conflict of interest

The authors declare no competing interest.

References

Abouelresh, M.O. An integrated characterization of the porosity in Qusaiba Shale, Saudi Arabia. J. Pet. Sci. Eng. 2017, 149: 75-87.

Bhargava, S., Awaja, F., Subasinghe, N. Characterisation of some Australian oil shale using thermal, X-ray and IR techniques. Fuel 2005, 84(6): 707-715.

Craddock, P.R., Prange, M.D., Pomerantz, A.E. Kerogen thermal maturity and content of organic-rich mudrocks determined using stochastic linear regression models applied to diffuse reflectance IR Fourier transform spectroscopy (DRIFTS). Org. Geochem. 2017, 110: 122-133.

Curtis, M.E., Sondergeld, C.H., Ambrose, R.J., et al. Microstructural investigation of gas shales in two and three dimensions using nanometer-scale resolution imaging. AAPG Bull. 2012, 96(4): 665-677.

Fleury, M., Romero-Sarmiento, M. Characterization of shales using T1-T2 NMR maps. J. Pet. Sci. Eng. 2016, 137: 55-62.

Dong, D.Z., Guan, Q.Z., Wang, S.F., et al. Shale gas in China: Reality and dream. Energy Explor. Exploit. 2015, 33(3): 397-418.

Gao, Z.Y., Fan, Y.P., Xuan, Q.X., et al. A review of shale pore structure evolution characteristics with increasing thermal maturities. Adv. Geo-Energy Res. 2020, 4(3): 247-259.

Gou, Q.Y., Xu, S., Hao F., et al. Full-scale pores and micro-fractures characterization using FE-SEM, gas adsorption, nano-CT and micro-CT: A case study of the Silurian Longmaxi Formation shale in the Fuling area, Sichuan Basin, China. Fuel 2019, 253: 167-179.

Gu, X., Cole, D.R., Rother, G., et al. Pores in Marcellus Shale: A neutron scattering and FIB-SEM study. Energy Fuels 2015, 29(3): 1295-1308.

Ibarra, J. Muñoz, E., Moliner, R. FTIR study of the evolution of coal structure during the coalification process. Org. Geochem. 1996, 24: 725-735.

Jaroniec, M., Avnir, D., An isotherm equation for adsorption on fractal surfaces of heterogeneous porous materials. Langmuir 1989, 5: 1431-1433.

Jarvie, D.M., Hill, R.J., Ruble, T.E., et al. Unconventional shale-gas systems: The mississippian barnett shale of north-central texas as one model for thermogenic shale-gas assessment. AAPG Bull. 2007, 91(4): 475-499.

Ji, W.M., Song, Y., Jiang, Z.X., et al. Fractal characteristics of nano-pores in the Lower Silurian Longmaxi shales from the Upper Yangtze Platform, south China. Mar. Pet. Geol. 2016, 78: 88-98.

John, M. Hunt. Petroleum Geochemistry and Geology, Second Edition. New York, USA, W. H. Freeman, 1996.

Ko, L.T., Loucks, R.G., Milliken, K.L., et al. Controls on pore types and pore-size distribution in the Upper Triassic Yanchang Formation, Ordos Basin, China: Implications for pore-evolution models of lacustrine mudrocks. Interpretation 2017, 5(2): 127-148.

Kong, S.Q., Huang, X., Li, K.J., et al. Adsorption/desorption

isotherms of CH_4 and C_2H_6 on typical shale samples. Fuel 2019, 255: 115632.

Li, K.J., Chen, G., Li, W., et al. Characterization of marine-terrigenous transitional Taiyuan formation shale reservoirs in Hedong coal field, China. Adv. Geo-Energy Res. 2018, 2(1): 72-85.

Li, K.J., Zeng, F.G., Cai, J.C., et al. Fractal characteristics of pores in Taiyuan formation shale from Hedong coal field, China. Fractals 2018a, 26(2): 1840006.

Li, K.J., Zeng, F.G., Sheng, G.L., et al. Investigation of fractal characteristics of taiyuan formation coal-shale from southern qinshui basin, china, by nitrogen adsorption and desorption analysis. J. Porous Media 2018b, 21(10): 929-951.

Li, X.H., Gao, Z.Y., Fang, S.Y., et al. Fractal characterization of nanopore structure in shale, tight sandstone and mudstone from the ordos basin of china using nitrogen adsorption. Energies 2019, 12(4): 583.

Li, X., Zeng, F.G., Wang, W., et al. FTIR characterization of structural evolution in low-middle rank coals. Journal of China Coal Society 2015, 40(32): 2900-2908. (in Chinese)

Lis, G.P., Mastalerz, M., Schimmelmann, A., et al. FTIR absorption indices for thermal maturity in comparison with vitrinite reflectance R0 in type-II kerogens from Devonian black shales. Org. Geochem. 2005, 36(11): 1533-1552.

Liu, X.F., Nie, B.S., Wang, W.X., et al. The use of AFM in quantitative analysis of pore characteristics in coal and coal-bearing shale. Mar. Pet. Geol. 2019, 105: 331-337.

Loucks, R.G., Reed, R.M., Ruppel, S.C., et al. Morphology, genesis, and distribution of nanometer-scale pores in siliceous mudstones of the Mississippian Barnett Shale. J. Sediment. Res. 2009, 79(12): 848-861.

Pfeiferper, P., Avnir, D. Chemistry nonintegral dimensions between two and three. J. Chem. Phys. 1983, 79: 3369-3558.

Rouquerol, J., Avnir, D., Fairbridge, C.W., et al. Recommendations for the characterization of porous solids (Technical Report). Pure Appl. Chem. 1994, 66(8): 1739-1758.

Shao, X.H., Pang, X.Q., Li, Q.W., et al. Pore structure and fractal characteristics of organic-rich shales: A case study of the lower Silurian Longmaxi shales in the Sichuan Basin, SW China. Mar. Pet. Geol. 2017, 80: 192-202.

Sheng, G.L., Su, Y.L., Wang, W.D. New fractal approach for describing induced fracture porosity/permeability/compressibility in stimulated unconventional reservoirrs. J. Pet. Sci. Eng. 2019, 179: 855-866.

Slatt, R.M., O''Brien, N.R. Pore types in the barnett and woodford gas shales: Contribution to understanding gas storage and migration pathways in fine-grained rocks.

AAPG Bull. 2011, 95: 2017-2030.

Sun, M.D., Yu, B.S., Hu, Q.H., et al. Nanoscale pore characteristics of the lower cambrian niutitang formation shale: A case study from Well Yuke #1 in the Southeast of Chongqing, China. Int. J. Coal Geol. 2016, 154-155: 16-29.

Wang, S.Q. Shale gas exploration and appraisal in China: Problems and discussion. Natural Gas Industry 2013, 33(12): 13-29. (in Chinese)

Wang, S.Y., Tang, Y.G., Schobert, H.H., et al. FTIR and ^{13}C NMR investigation of coal component of late permian coals from Southern China. Energy Fuels 2011, 25(12): 5672-5677.

Wood, D.A., Hazra, B. Pyrolysis S2-peak characteristics of raniganj shales (India) reflect complex combinations of kerogen kinetics and other processes related to different levels of thermal maturity. Adv. Geo-Energy Res. 2018, 2(4): 343-368.

Yang, F., Ning, Z.F., Liu, H.Q. Fractal characteristics of shales from a shale gas reservoir in the Sichuan Basin, China. Fuel 2014, 115: 378-384.

Yang, F., Ning, Z.F., Wang, Q., et al. Pore structure characteristics of lower Silurian shales in the southern Sichuan Basin, China: Insights to pore development and gas storage mechanism. Int. J. Coal Geol. 2016, 156: 12-24.

Yang, R., He, S., Yi, J.Z., et al. Nano-scale pore structure and fractal dimension of organic-rich Wufeng-Longmaxi shale from Jiaoshiba area, Sichuan Basin: Investigations using FE-SEM, gas adsorption and helium pycnometry. Mar. Pet. Geol. 2016, 70: 27-45.

Zhang, J.C., Fan, T.L., Li, J., et al. Characterization of the Lower Cambrian Shale in the northwestern Guizhou province, south China: Implications for shale-gas potential. Energy Fuels 2015, 29(10): 6383-6393.

Zhang, Q., Liu, R.H., Pang, Z.L., et al. Characterization of microscopic pore structures in Lower Silurian black shale (S1l), southeastern Chongqing, China. Mar. Pet. Geol. 2016, 71: 250-259.

Zhou, L., Kang, Z.H. Fractal characterization of pores in shales using NMR: A case study from the Lower Cambrian Niutitang Formation in the Middle Yangtze Platform, Southwest China. J. Nat. Gas Sci. Eng. 2016, 35: 860-872.

Zou, C.N., Dong, D.Z., Wang, Y.M., et al. Shale gas in China: Characteristics, challenges and prospects (II). Pet. Explor. Dev. 2016, 43(2): 182-196.

Zou, C.N., Yang, Z., Huang, S.P., et al. Resource types, formation, distribution and prospects of coal-measure gas. Pet. Explor. Dev. 2019, 46(3): 451-462.